Chapter 1

Introduction and Literature survey

1.1 Introduction

In recent years, advancements in aerospace and transportation industries have heightened the demand for reduced energy consumption, creating significant challenges for environmental protection[1,2]. Achieving lightweight designs in automobiles and aircraft has proven to be an effective strategy for addressing these issues[3,4]. Al alloys, with a density roughly one-third that of steel, offer advantages such as high specific strength, stiffness, and excellent corrosion resistance[5]. These properties not only contribute to reducing the weight and energy consumption of products but also fulfill diverse production and operational requirements[6,7]. Consequently, aluminum alloys have become essential materials for large structural components in construction, vehicles, aerospace, and rail transportation. A common application includes aluminum alloy hubs and rims. As the integration of aluminum alloys in automotive manufacturing becomes unavoidable, their ability to endure cyclic loading renders fatigue performance a critical property to evaluate[8]. 7075 Al alloy is widely utilized in the aerospace and automotive industries due to its unique combination of properties[9]. Materials used in these sectors often require attributes such as high strength-to-weight ratio, excellent corrosion resistance, fracture toughness, good formability, weldability, and machinability[10].

1.1.1 Basic study of aluminium alloy

For more than eight decades, aluminum alloys have been widely acknowledged as superior materials for use in aircraft structural applications [11]. Among various metals,

aluminum alloys are distinguished by their low density and excellent mechanical properties, which make them highly suitable for engineering applications, particularly in the aerospace industry [12]. As illustrated in Fig. 1.1,[13] Aluminum alloys are broadly classified based on their composition and processing methods. In aerospace applications, aluminum accounts for approximately 80% of the total structural weight. This widespread use is attributed to its exceptional strength-to-weight ratio and inherent corrosion resistance, both of which are critical for ensuring the structural integrity of the aircraft and the safety of its occupants [14]. However, aluminum alloys exhibit a high susceptibility to corrosion, necessitating the application of surface treatments such as plasma electrolytic oxidation, anodic oxidation, and protective coatings to enhance their corrosion resistance and extend their service life [15,16]. Throughout their operational lifespan, engineering components are subjected to a variety of stress conditions, among which fatigue loading is particularly detrimental. Under cyclic loading, materials can experience failure even when the applied stresses remain below the yield strength, making fatigue a critical consideration in the design and performance assessment of structural components [8].

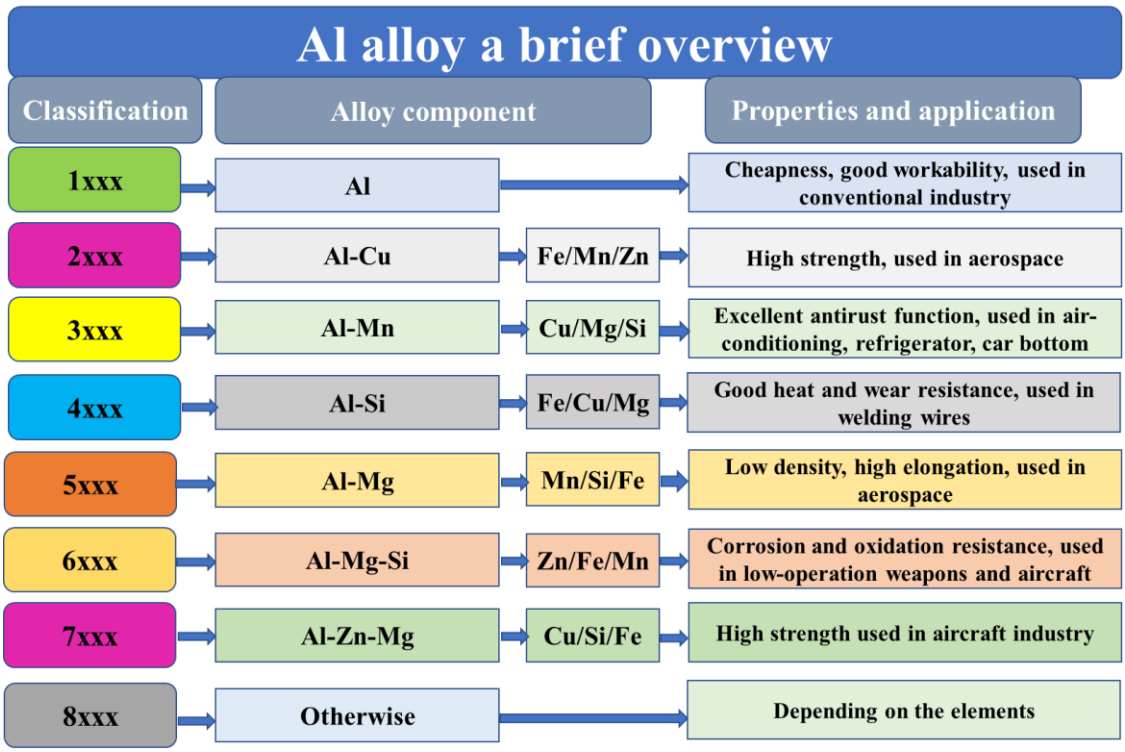

Fig. 1.1. A comprehensive classification of Al alloys[13].

1.1.2 7075 Al alloy

The 7075 aluminum alloy (The composition is as follows (wt.%): Zn – 5.6, Mg – 2.5, Cu – 1.6, Cr – 0.23, Fe – 0.2, Si – 0.12, Mn – 0.1, Ti – 0.06, and balance Al.), renowned for its age-hardening capabilities, possesses several advantageous properties, including low density, high specific strength, excellent mechanical resilience, good formability, and cost-effectiveness [17,18]. The 7075 aluminum alloy is renowned for its exceptional strength-to-weight ratio, rendering it a preferred material in structural and aerospace engineering applications (Fig. 1.2), particularly in the fabrication of aircraft wings and fuselage components. Its combination of high strength and low density also makes it suitable for use in a range of other applications, including rock-climbing equipment and bicycle components[19]. Widely recognized by experts across various disciplines, 7075 aluminum alloy is extensively employed in sectors such as

aerospace, aviation, and transportation industries that demand lightweight yet high-strength structural materials[20].

Chemically, 7075 is an aluminum alloy in which zinc serves as the principal alloying element. It is characterized by high fatigue strength and moderate machinability; however, it exhibits comparatively lower weldability and corrosion resistance relative to other aluminum alloys. Like all aluminum-based materials, 7075 has a specific gravity of 2.73 (0.098 lb/in^3)[21].

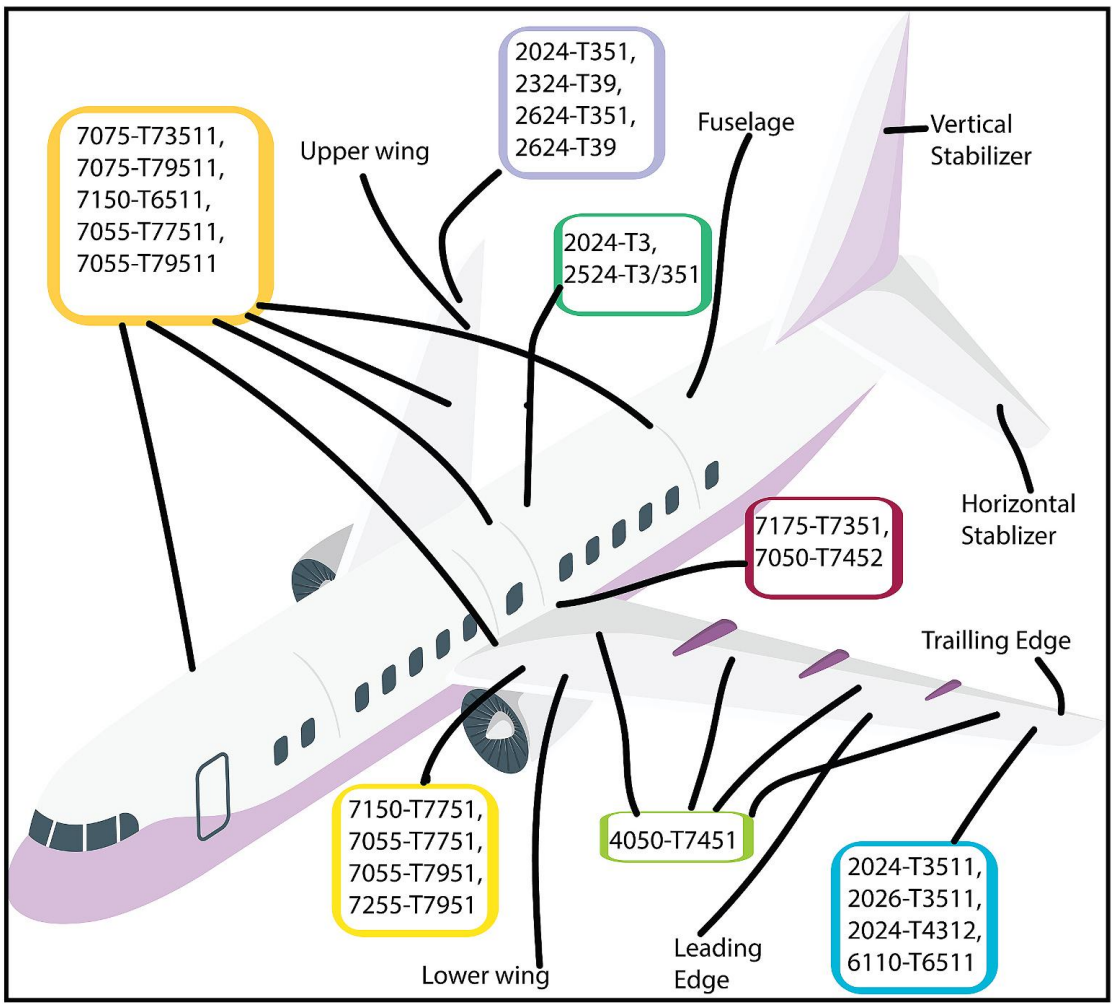

Fig. 1.2 Application of 7075 Al alloy in aviation[22]

1.2 Cold rolling of 7075 Al alloy

The widespread application of 7075 aluminum alloy is constrained by its limited cold-forming ability and the complexity and high cost associated with hot-forming processes [23]. Currently, Al-Zn-Mg-Cu alloy sheets are employed in aircraft applications primarily in the form of thick plates, eliminating the need for complex forming processes [24]. Therefore, enhancing the cold-rolling capability and mechanical properties of Al-Zn-Mg-Cu-based alloys is essential to fully exploit their potential in improving safety, reducing structural weight, enhancing fuel efficiency, and broadening their application range. However, cold rolling of the 7075 aluminum alloy presents significant challenges due to its comparatively high hardness among aluminum alloys. Conventionally, 7075 alloy sheets have been processed through hot rolling from an initial thickness of 30 mm to 1 mm at 400 °C to prevent cracking, as direct cold rolling tends to cause structural damage. Notably, the incorporation of ZnO nanoparticles enabled the alloy to withstand up to 90% cold reduction, indicating improved cold-rolling performance [23]. To date, a maximum deformation of approximately 50–60% has been achieved through cold rolling in 7075 aluminum alloy [25]. A deformation of 70% was attained in the 7075 aluminum alloy through cryo-rolling [26].

J.G. Jeon et al;[23]made an attempt to cold rolled the conventional 7075 aluminum alloy; however, the process could only achieve a maximum deformation of 50% before failure. To overcome this limitation, a modified alloy designated as I-7075 Al was developed. This alloy was engineered by introducing decomposed oxygen atoms derived from nano-sized ZnO particles into the 7075 Al matrix using a non-metallic alloying technique.

Figure 1.3 presents a comparative analysis of the cold rolling behavior of both 7075 and I-7075 Al alloys. Initially, both alloy sheets exhibited satisfactory surface integrity with only minor cracking following hot rolling to a thickness of 10 mm. Upon further reduction to 7 mm, the conventional 7075 Al alloy developed prominent cracks oriented perpendicular to the rolling direction (Fig. 1.3(a)). In contrast, the I-7075 Al alloy maintained structural integrity with only minimal edge cracking even at a reduced thickness of 5 mm (Fig. 1.3(b)). As a result, it was possible to fabricate a cold-rolled sheet with a final thickness of 1 mm exclusively from the I-7075 Al alloy.

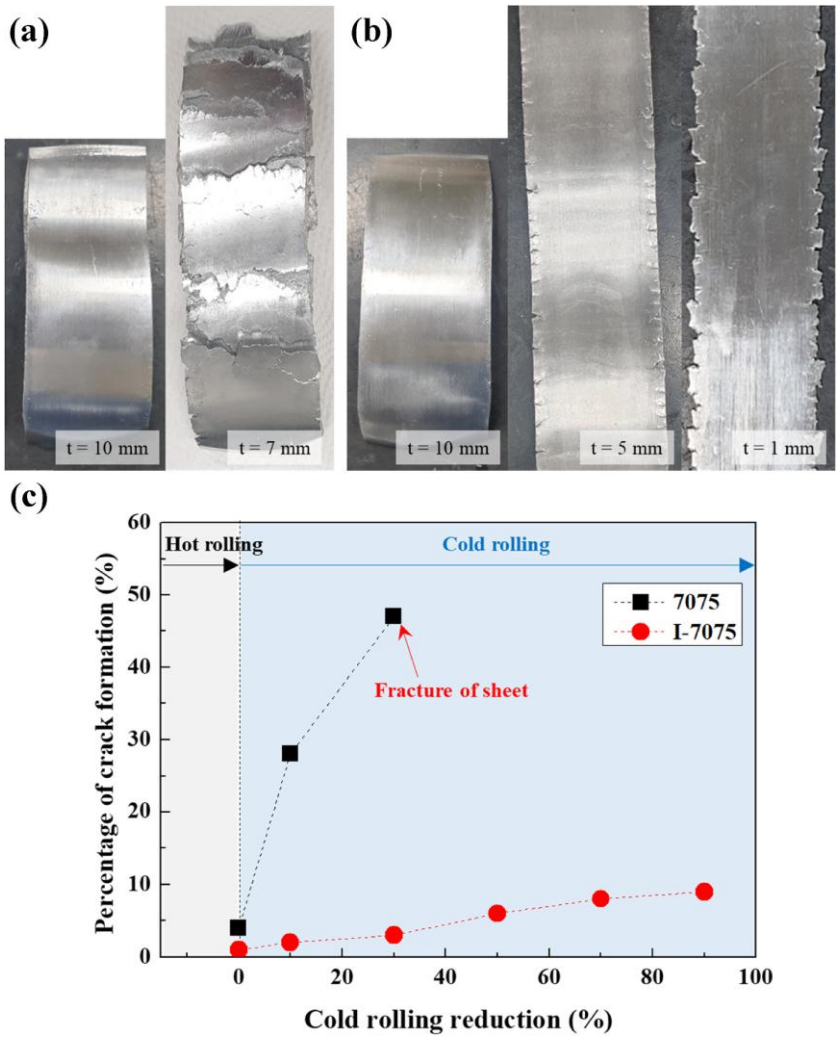

Fig. 1.3 (a) and (b) show images of 7075 and I-7075 aluminum alloy sheets during the cold rolling process, respectively. (c) illustrates the cold rolling performance of the alloy sheets[23].

Fig.1.4 illustrates the schematic of the decomposition and reaction process between ZnO nanoparticles and the Al melt. When loosely agglomerated ZnO nanoparticles with a surface curvature of around 20 nm come into contact with the Al melt, they undergo decomposition driven by interdiffusion between Al and Zn atoms. This interdiffusion is facilitated by the high chemical potential energy resulting from the nanoparticles' extremely small surface curvature, which enhances atomic mobility.

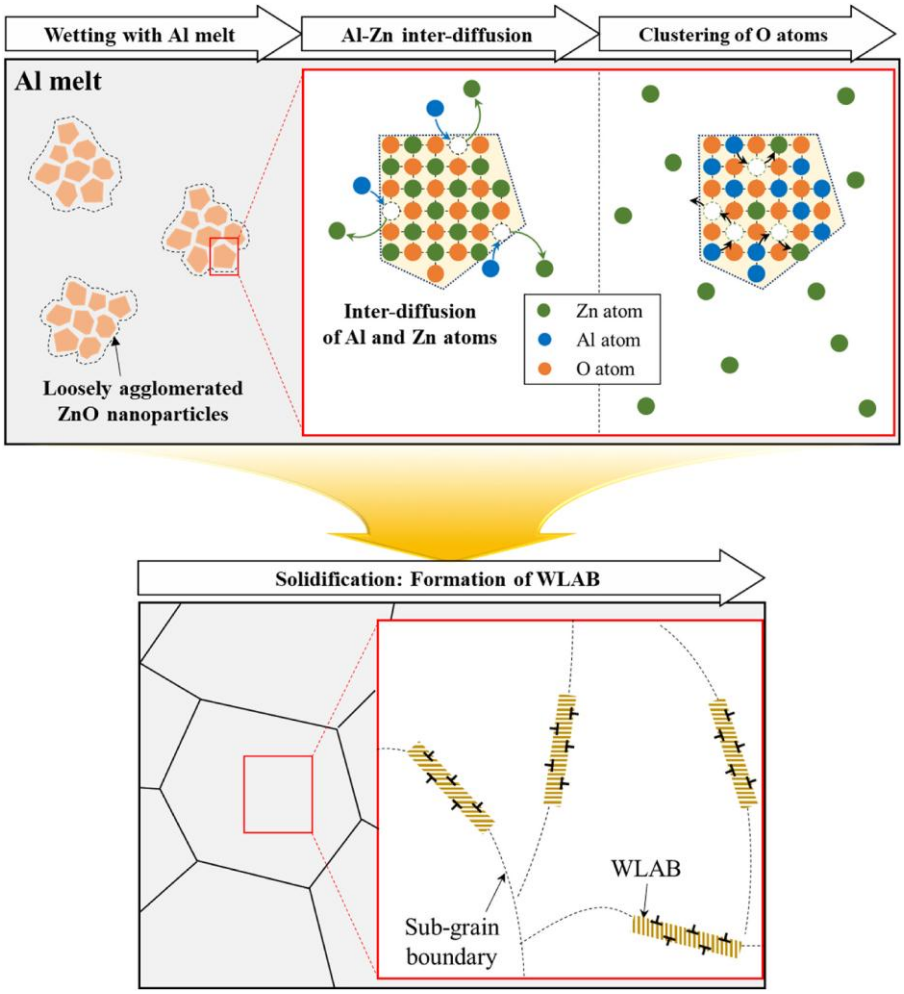

Fig. 1.4 A schematic representation of the decomposition and interaction between ZnO nanoparticles and molten aluminum[23].

Fig 1.5 schematically illustrates the role of wide low-angle boundaries (WLABs) during plastic deformation. In the I-7075 aluminum alloy, aluminum-oxygen nanoclusters act as WLABs and are located along sub-grain boundaries formed during solidification.

These WLABs inherently contain pre-existing dislocations (as shown in Fig. 1.5), which can glide easily along slip planes in the early stages of plastic deformation. During this process, the WLABs function both as sources and sinks for dislocations, facilitating the continuous generation and absorption of additional dislocations. A significant accumulation of activated dislocations occurs at the interfaces of adjacent WLABs, leading to the development of secondary dislocation walls and eventually forming a dense dislocation network. In contrast, the conventional 7075 Al alloy lacking WLABs exhibits dislocation interactions predominantly with high-angle grain boundaries and existing dislocations, resulting in the formation of relatively coarse dislocation cells. Consequently, the I-7075 alloy, characterized by its WLAB-induced refinement of dislocation cells to approximately 500 nm, demonstrates improved elongation due to its enhanced dislocation storage capability.

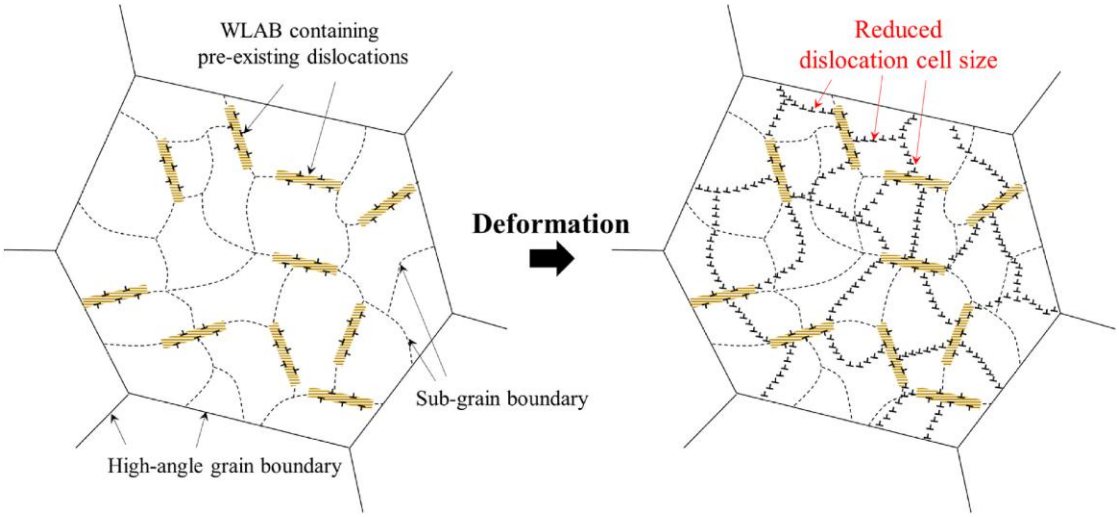

Fig. 1.5 Schematic illustration of the mechanism by which WLABs contribute to the reduction of dislocation cell size during plastic deformation[23].

Broad Al–O nanoclusters (~40 nm wide) were present at the sub-grain borders, causing sub-grains smaller than 1 μm to develop upon solidification. By adding many pre-existing dislocations, these clusters allowed for lattice mismatch between the matrix

and the Al–O phase. They also served as dislocation cells during plastic deformation, increasing the alloy's capacity to store dislocations. Consequently, a notable cold rolling reduction of up to 90% was made possible by the homogenized I-7075 alloy's high elongation of roughly 20%. The I-7075 sheet's recrystallized grain size was reduced to 20.1 μm by this lengthy cold treatment, which is significantly finer than the 34.2 μm grain size seen in hot-rolled 7075 sheets. During deformation, the Al–O nanoclusters were crucial, which resulted in a noticeable improvement in ductility. In particular, compared to their hot-rolled 7075 counterparts, the recrystallized and T6-aged I-7075 alloy sheets' elongation increased by roughly 40% and 50%, respectively [23].

1.3 Precipitation strengthening of 7075 Al alloy

Precipitates have a significant impact on the final characteristics of the age-hardened 7075 Al alloy. The precipitation mechanisms in the 7xxx series Al alloy have been the subject of much study throughout the years [27]. The precipitation patterns of Al–Zn–Mg alloys are significantly impacted by the various heat treatment settings used [28,29]. Furthermore, the mechanical properties of the alloys are significantly influenced by the type, quantity, and size of the precipitated phases [30,31]. The precipitation sequence observed during artificial aging of Al–Zn–Mg alloy typically involves the transition from α (supersaturated solid solution) to GP(Guinier–Preston) zones, followed by the emergence of η"(eta double prime) phase afterwards η'(eta prime) and eventually the formation of η(eta) (SSSS -> GP zones/atomic clusters -> η" (eta double prime) -> η' (eta prime) -> η (eta),) phase[29,32]. Heat treatment of the surface Strengthening successfully modifies these precipitates' amount, size, and dispersion. The most sought-after phase is the η" metastable phase since it has the strongest effect. It should be noted, nonetheless, that the simplified precipitation order disregards the impact of extra phases

or modifications in chemical composition that could alter or quicken the sequence [33]. Many researchers have studied about η and η' precipitates thoroughly[34–37] but very less study is found regarding η'' precipitate[38]. During the controlled heat treatment process, various other types of precipitates like T (Al_2 Mg_3 Zn_3), S (Al_2 CuMg), and θ (Al_2 Cu) phases [14,15][38] form progressively within the Al-Zn-Mg-Cu matrix in very small amount, leading to notable changes in both the strength and ductility of the material.

J.W. Jin et al;[39] examined how precipitation affected tiredness life.Suzhou Hairun Metal Materials Co., Ltd. provided the commercial 7075-T7651 high-strength aluminium alloy (composition: Al-5.69Zn-2.58Mg-1.47Cu-0.21Cr-0.18Fe-0.12Mn-0.08Si-0.06Ti) utilised in this investigation. The alloy sheets were 10 μm thick. Thermo-mechanical treatment (TMT) procedures that combined traditional rolling and heat treatment were used to customise the microstructure. The materials were separated into three categories: 7075-Min, 7075-Mid, and 7075-Max, based on the average grain sizes that were obtained. Figure 1.6 lists certain TMT process parameters. The XRD examination of samples of 7075 Al alloy under various heat treatment settings is shown in Fig. 1.7. Al, Al_2 Cu, and $MgZn_2$ are among the phases that have been identified. The as-received, solution-treated with cyclic loading, and T6 states exhibit noTable differences in diffraction peak intensities. The Al phase continuously shows the highest peak intensity among the three circumstances. The Al_2 Cu and $MgZn_2$ phases exhibit comparatively high peak intensities in the as-received condition, however these precipitate peak intensities are decreased in the solution-treated with cyclic loading state [40].

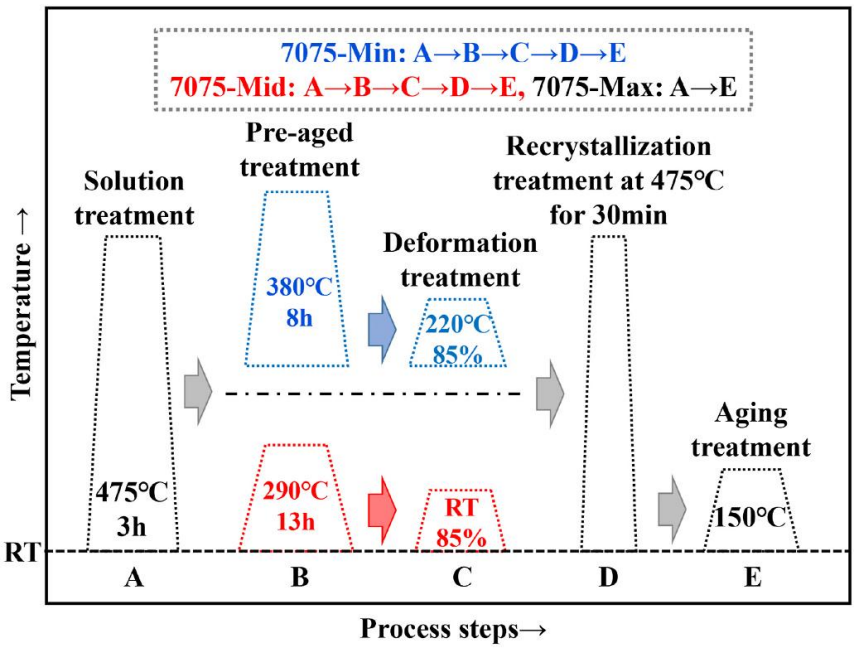

Fig.1.6 Thermo-mechanical treatment (TMT) processes parameters[39]

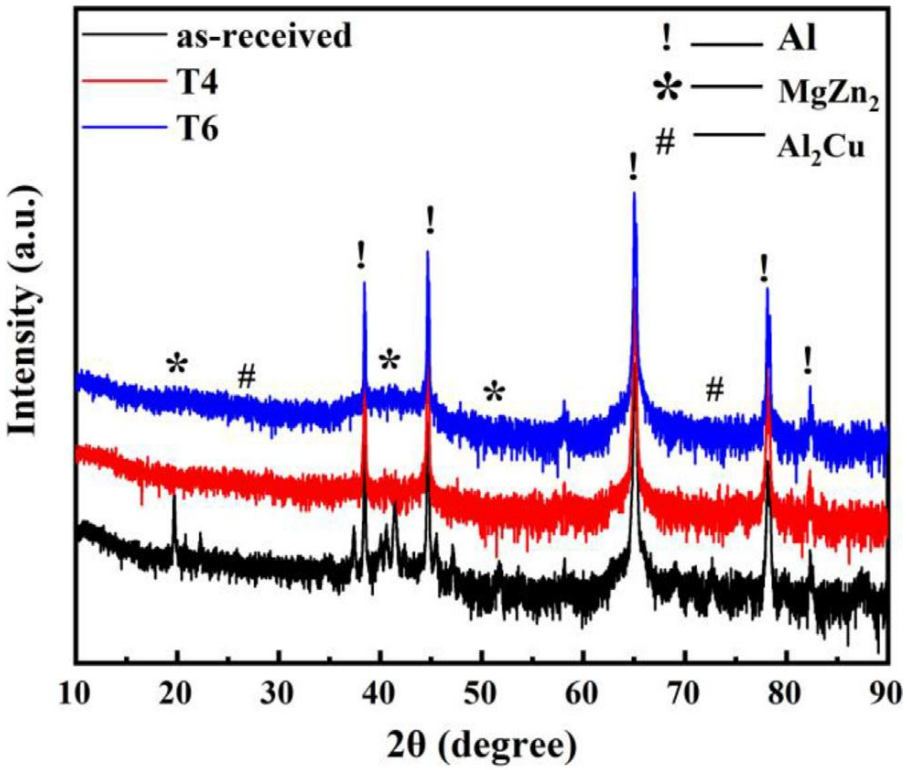

Fig.1.7 XRD analysis of 7075 aluminum alloy under various heat treatment conditions[40].

Fig. 1.8 shows the TEM picture of a solution that has been heat treated. The 7075 Al alloy is under-aged (UA) at 150 ◦C for two hours, peak-aged (PA) at 150 ◦C for eight hours, and over-aged (OA) at 150 ◦C for 204 hours. As seen in Fig. 1.8(a), the high-density dislocations vanish during solution treatment, leading to the development of distinct grain boundaries. A comparatively distinct precipitation-free zone (PFZ) forms close to the grain boundaries after ageing treatment. Grain boundary precipitates (GBPs) and intragranular precipitates (IPs) progressively grow in size as ageing time increases. The usual $MgZn_2$ strengthening phase in 7075 Al alloy is the intragranular precipitates (Ips) [41], show, using Image Pro Plus software, diameters of 0.38 ± 0.12 nm, 0.72 ± 0.18 nm, and 2.34 ± 0.21 nm in the UA, PA, and OA phases, respectively. Additionally, as ageing time increases, the GBPs' aspect ratio likewise rises [39].

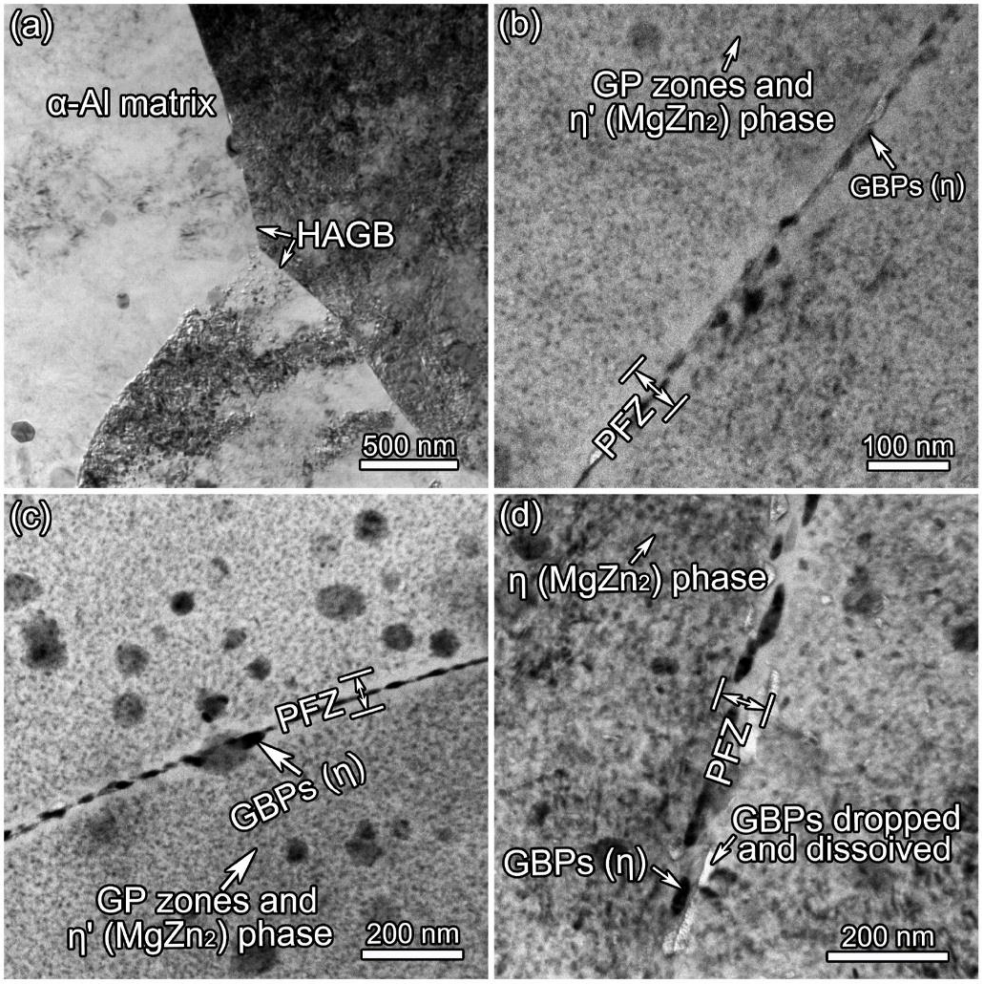

Fig. 1.8 TEM microstructures of 7075 Al alloy. (a) After solution treatment, (b–d) UA state (150 ◦C 2h), PA state (150 ◦C 8h) and OA state (150 ◦C 204h), respectively[39].

Since the morphology, size, and density of the precipitated phases significantly affect the alloy's properties, Gong B et al;[42] examined the microstructure of the samples at various aging durations using TEM, as shown in Fig. 1.9. Figs. 1.9 (a) to (c) reveal that the precipitate size gradually increases with aging time, while the number density initially rises and then declines. Based on these observations, it can be inferred that aging at 120 ◦C for 8 h, 24 h, and 48 h in an oil bath furnace corresponds to the UA, PA, and OA states of the alloy, respectively. Figure 1.9(d) provides a quantitative analysis of the average size and number density of the precipitates across different aging

conditions. The average sizes of the precipitates for the UA, PA, and OA states are approximately 6 nm, 7 nm, and 8 nm, respectively[42].

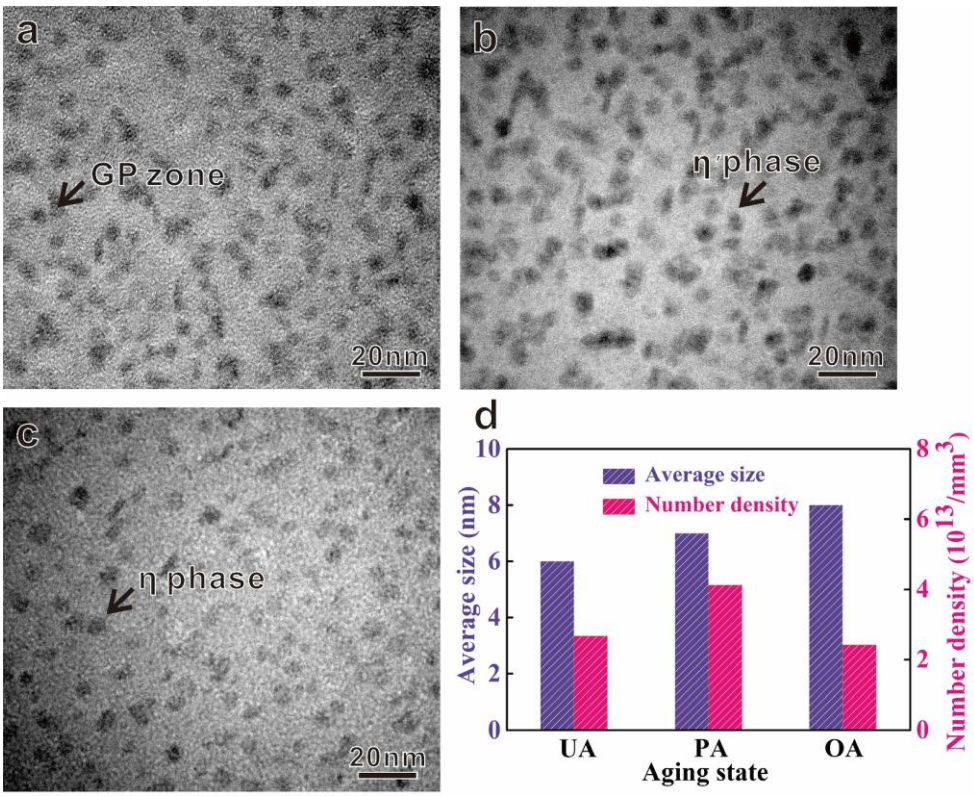

Fig. 1.9 The matrix precipitates of 7075 at different aging times. (a) 8 h; (b) 24 h; (c) 48 h; (d) average size and number density of precipitated phases at different aging states[42]**.**

Fig. 1.10 presents TEM images of the 7075 Al alloy subjected to different heat treatment conditions. Figs. 1.10 (a) and 1.10 (b) correspond to the alloy after solution treatment followed by cyclic loading, and in the T6 condition, respectively. In both cases, the precipitates exhibit similar morphologies, primarily spherical and rod-like shapes. However, the precipitate size differs: in the solution-treated and cyclically loaded condition, the precipitates range from 150 to 250 nm, whereas in the T6 condition, they are smaller, measuring less than 100 nm. Despite their smaller size, the precipitate density is significantly higher in the T6 condition compared to the solution

treatment + cyclic loading condition. This difference in precipitate characteristics may influence the mechanical strength and fatigue fracture behavior of the respective specimens. Figs. 1.10 (c) and 1.10 (d) display high-resolution TEM (HRTEM) and selected area electron diffraction (SAED) patterns taken along the <110>Al and <112>Al crystallographic directions of the matrix. These observations suggest that the fine precipitates are composed of the $MgZn_2$ phase[40].

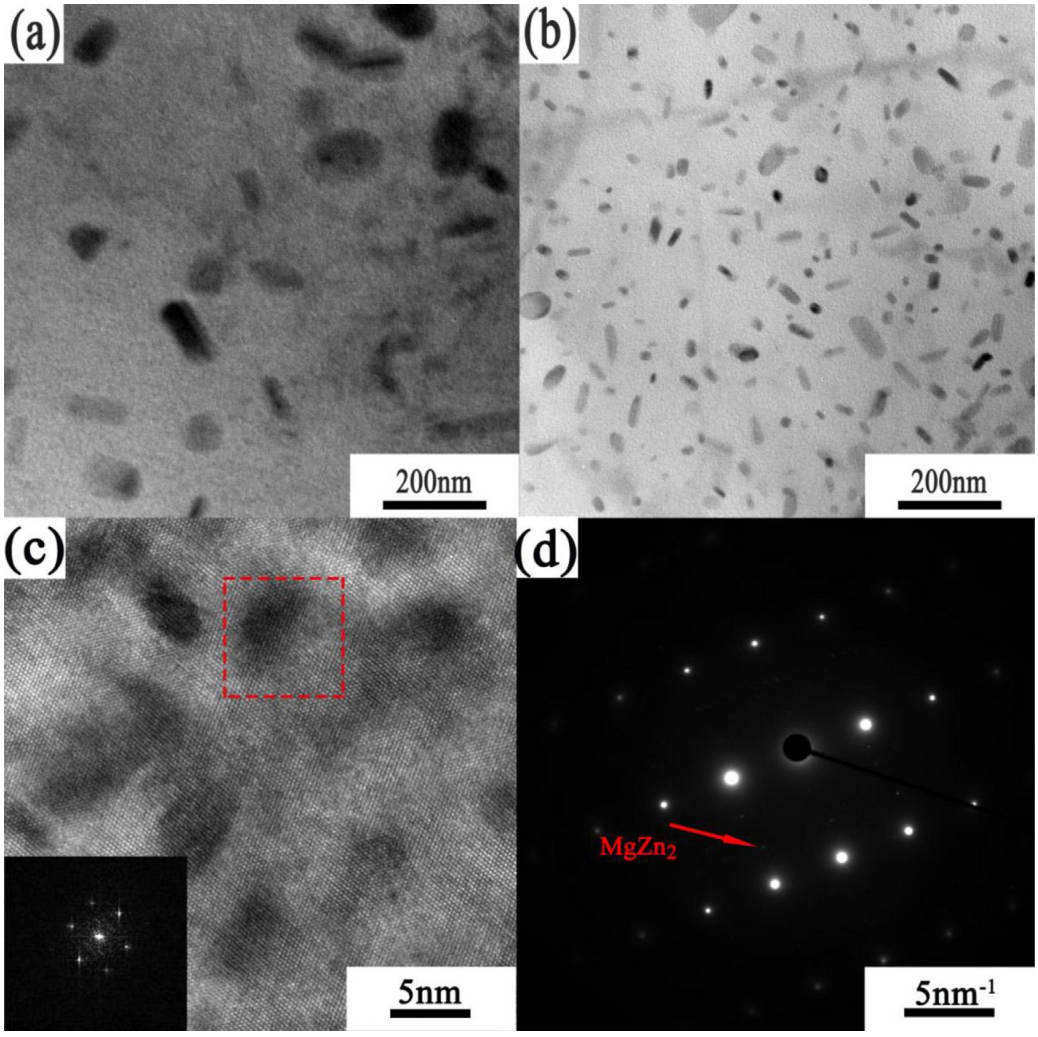

Fig. 1.10 TEM images of the 7075 Al alloy: (a) after solution treatment followed by cyclic loading; (b) in the T6 condition; (c) high-resolution TEM (HRTEM) image along the <110>Al zone axis; (d) selected area electron diffraction (SAED) pattern along the <112>Al zone axis[40].

1.4 Fatigue crack growth study of 7075 Al alloy

As aerospace has grown in importance around the world in recent years, rivalry in this industry has also ramped up, putting additional demands on the precision and integrity of structural components for aircraft and space craft [43]. Aircraft structures experience varying stress levels during take-offs, landings, turbulence, and other operational conditions. These repetitive stress cycles cause microscopic cracks to form and propagate over time[44,45]. Initially, small cracks or flaws may form in areas with stress concentrations, such as joints, fastener holes, or sharp corners. These can originate from manufacturing defects, material imperfections, or surface damage [26,46]. These can result in significant fatigue-related deterioration under fluctuating loads. Data indicates that over 60% to 80% of failures in aircraft structural components occurring due to fatigue failure [47,48]. Thus, enhancing the fatigue resistance of aerospace components emerges as a crucial objective. The fatigue crack growth (FCG) behavior of Al alloys is affected by several factors, including load conditions and material properties[49,50]. These material properties encompass alloy composition where an increase in copper content can accelerate FCG[51]. Table 1.1 is showing literature review of fatigue crack growth rate test of 7075 Al alloy

Table 1.1: Literature review of 7075 Al alloy for fatigue crack growth rate test

Author	**Material**	**Findings**
Ayush Joshi et al;[52]	7075-T651 Al alloy	• This study demonstrated that a suiTable post-heat treatment process can nearly restore the tensile properties of friction stir welded 7075-T651 Al alloy. • There is a negligible effect on the Paris crack growth parameters for natural aged and HT1 (190°C for 24 h aging) conditions, • while HT2(430°C for 12 h aging) post-weld heat treatment results in a slightly higher exponent for both welded and base metal.
Ping Zhang et al;[53]	7075 aluminum alloy	• Water jet (WJ) enhancement induces residual compressive stresses that suppress fatigue crack growth, while higher jet velocity increases fatigue life cycles but also leads to greater surface roughness.
Luyi Han et al;[54]	Al-Zn-Mg-Cu alloy	• An in-situ study examines slip system activation, intergranular plasticity transfer, and deformation heterogeneity in the Al-Zn-Mg-Cu alloy. • Finding revealed that the deformation heterogeneity behavior of Al-Zn-Mg-Cu alloy was closely linked to the activation of slip systems and the transfer of plasticity at grain interfaces. • This study's comprehensive analysis revealed that plasticity transfer occurs between grains that simultaneously possess high geometric compatibility factors and low residual dislocation values.
K.F. Walker et al;[55]	aluminium alloy 7075-T7351	• The study examines the fatigue crack growth in aluminum alloy 7075-T7351 under spike overload and aircraft spectrum loading through simulation. • The finding shows that enhanced model successfully predicted crack growth within approximately ±30% of the observed values. • The enhanced modeling approach developed in this study has enabled aircraft structural integrity program managers to reduce the uncertainty factors applied in crack growth predictions.

S M Ghalehbandi et al;[56]	7075 Al alloy after	• The hardness and tensile mechanical properties of solutionized 7075 aluminum alloy were significantly enhanced through a single-pass ECAP (equal channel angular pressing) process followed by natural aging. • Artificial aging after ECAP has reduced the alloy's FCGR due to the precipitation of coherent particles.
Tianwen Zhao et al;[57]	7075-T651 aluminum alloy	• The adapted Wheeler's model successfully predicts fatigue crack growth under overload and high–low loading. A single overload or reduced amplitude markedly decreases crack growth rate, whereas a single underload has little effect.
Ivo Černý et al;[58]	7075 Al-alloy type	• The growth of short fatigue cracks in a 7075-type aluminum alloy is investigated following shot peening. • The direct current potential drop (DCPD) method was successfully adapted and validated as the most suitable approach due to its capability to detect short cracks of approximately 0.2 mm in length and its ability to assess the average crack length, including the crack front within the specimen. • The slowdown in crack growth was notably pronounced, especially for cracks smaller than 2 mm.
Mustafa M. Kadhim et al;[59]	Al 7075-T6	• The results demonstrated that incorporating MWCNTs (multi-walled carbon nanotubes) significantly reduces the crack growth rate while enhancing fatigue life, hardness, stiffness, yield strength, and ultimate tensile stress. • The crack growth resistance improves by 83.5% and 81.6% compared to the uncoated specimens.
H. Quan et al;[60]	7075-T6	• This research is concluded that both the total plastic dissipation per cycle and the plastic dissipation in the reversed plastic zone exhibit a nonlinear relationship with da/dN (rate of change of crack length per cycle) for 7075-T6.

		• The relationship between dW/dN (total plastic dissipation per cycle) and da/dN varies depending on the stress ratio. • When the exponent in Paris' equation approaches 4, the plastic dissipation can be considered approximately linear in relation to the fatigue crack growth rate.

K.F Walker et al; [55] did a comparative study on the fatigue crack growth behavior of a third-generation Al-Li alloy (AA2198-T8) and a conventional aerospace aluminum alloy (AA2024-T3). The fatigue crack growth history was reconstructed using marker band loading sequences involving two different R-ratios. The influence of alloy composition and loading orientation relative to the rolling direction was analyzed through distinct differences observed in the fracture surface morphologies of the two alloys. Marker bands helped pinpoint the likely crack initiation sites and assisted in estimating the crack growth rates. Additionally, a data reduction method was employed to determine the number of cycles required for crack initiation.

Fig. 1.11 shows the fatigue fracture surface of Specimen 05, which was tested under constant amplitude (CA) loading at an R-ratio of 0 and a maximum stress (Smax) of 75 MPa, with overloads of factor 2.0 applied at crack lengths of 30 mm and 50 mm from tip to tip.

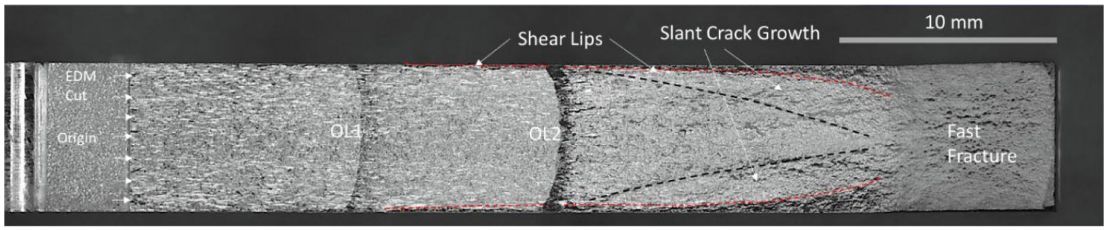

(a)

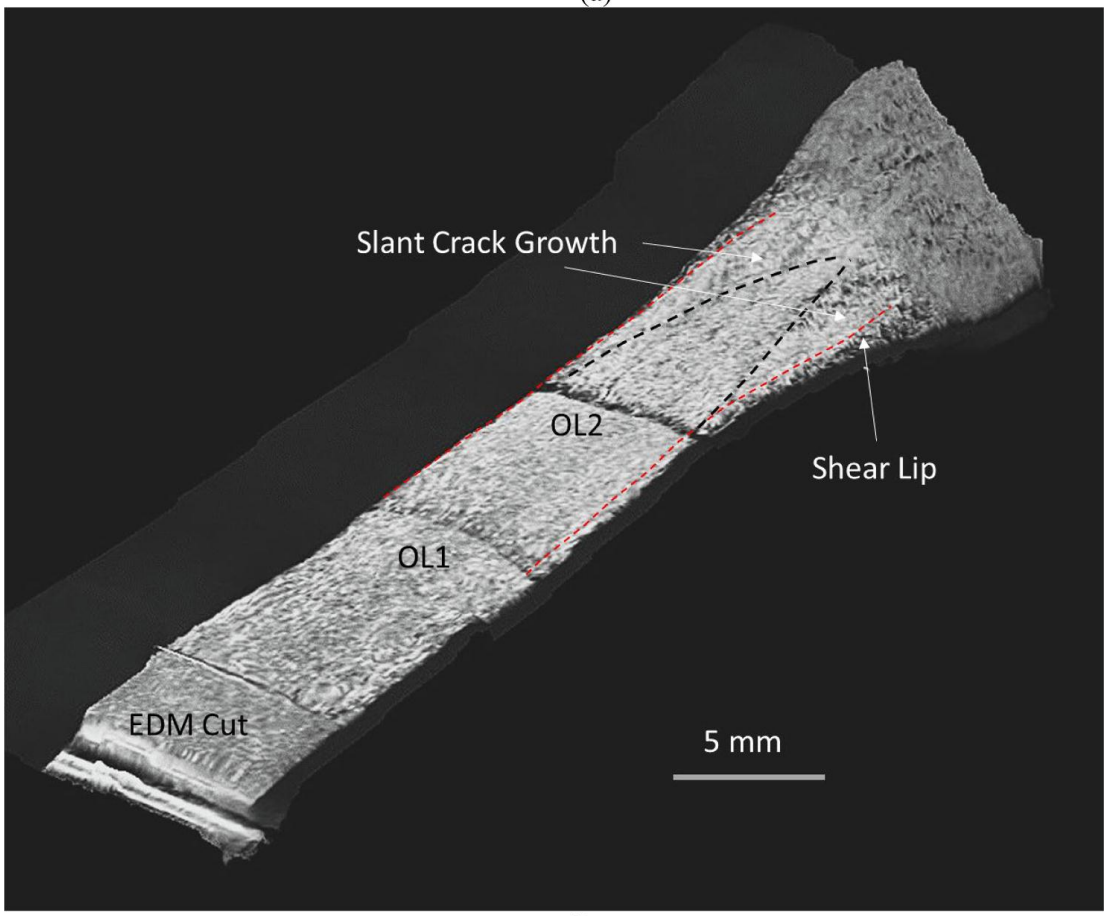

(b)

Fig. 1.11 Fatigue fracture surface of Specimen 05 tested under constant amplitude (CA) loading with a stress ratio **R = 0** and maximum stress **S= 75 MPa**, including factor 2.0 overloads applied at crack lengths of 30 mm and 50 mm (tip-to-tip). (a) Top-down view of the fatigue fracture surface. (b) 3D view highlighting overload-induced markings and the transition zones from flat (plane strain) to slant (plane stress) fracture morphology [55].

The model predictions of crack-opening load, evaluated under constant amplitude loading at R = 0 (Specimen 03), are presented in Fig. 1.11, alongside the experimental results. A top-down view of the fracture surface, scaled to match the horizontal axis of

the graph, is also included. Crack-opening loads were determined using the offset-compliance method in accordance with ASTM E-647 [57], which defines the procedure for calculating the 1% and 2% offset values. The crack-opening load (OP_0) was estimated by linear extrapolation from these offsets using equation (1):

$$OP_0 = 2OP_1 - OP_2 . \quad (1)$$

Despite noticeable scatter in the experimental data, a clear trend of increasing crack-opening load ratio is observed from c/w = 0.4 onward. This increase correlates with the development of shear lips on the specimen surfaces, as seen in the fracture surface image in Fig. 1.12(a). The formation of shear lips also leads to deviation in the surface crack path, illustrated in Fig. 1.12(b), and aligns with the measured increase in crack-opening load. The shift from flat to slanted fracture behavior is visible in Fig. 1.12(c). The FASTRAN model results closely follow the experimental trend and show good agreement with the observed fatigue fracture characteristics.

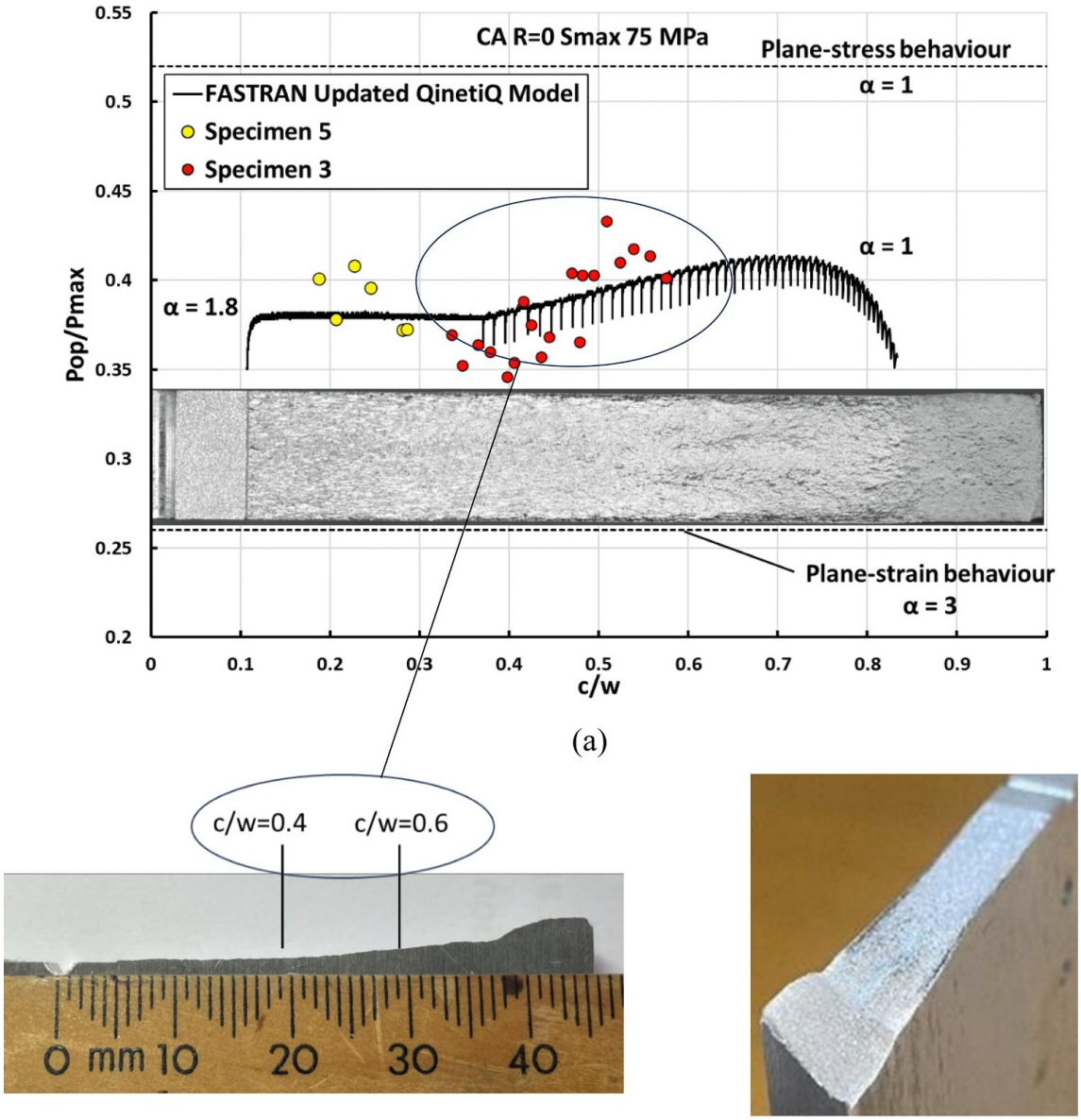

Fig. 1.12 Comparison of crack opening measurements with experimental results under constant amplitude loading at R = 0. (a) Crack opening measurements. (b) Front face of the specimen illustrating crack path deviation due to shear lip formation and the increase in crack opening load in the range of c/w = 0.4 to 0.6. (c) Fracture surface on one side of the specimen[55].

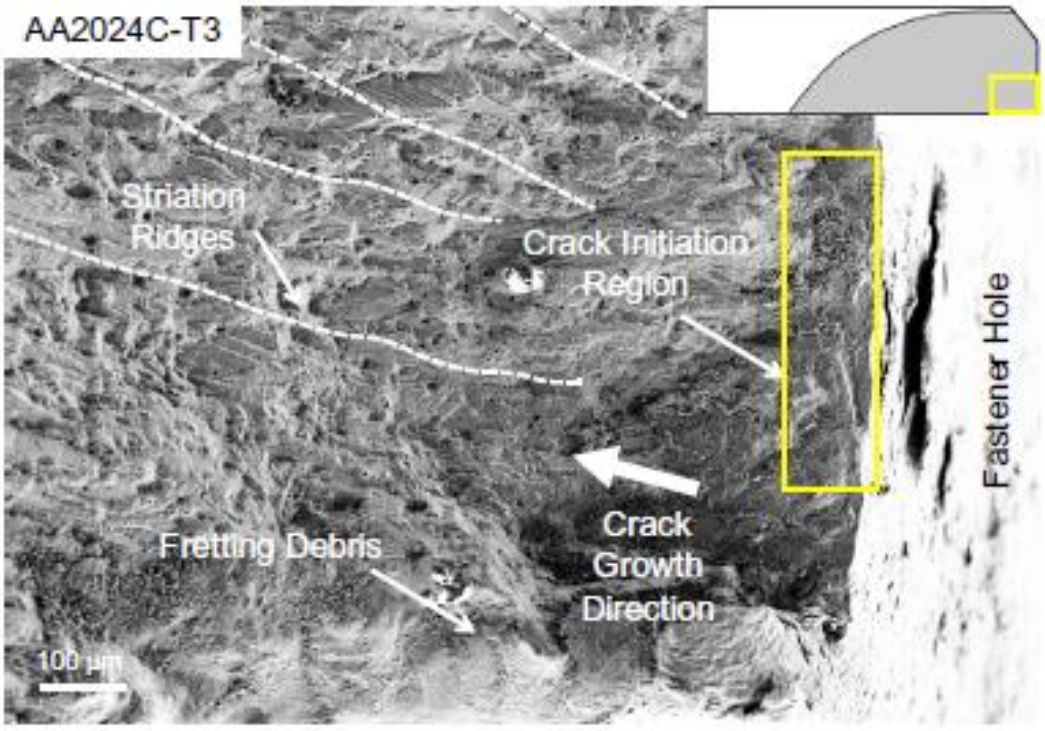

Fig. 1.13 A crack initiation zone (marked by the solid rectangle) in AA2024C-T3 'LT' is located at the interface between the aluminum matrix and the clad layer, adjacent to the fastener bore hole, as indicated by the presence of striation ridges (outlined by dashed lines) and fretting debris[61].

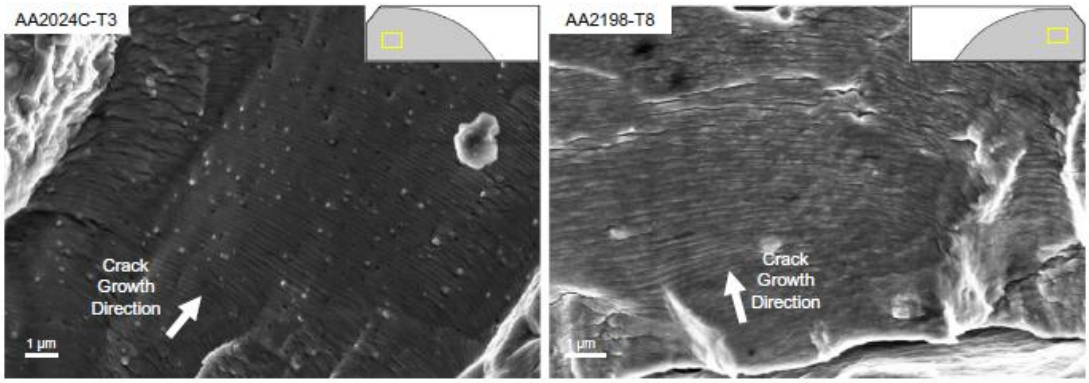

Fig. 1.14 Representative fatigue fracture zones (FFZs) displaying striation markings oriented perpendicular to the crack propagation direction in AA2024C-T3 'L' (left) and AA2198-T8 'L' (right)[61].

Two distinct regions were clearly observed on either side of the fastener hole in each specimen. One of these is the fatigue fracture zone (FFZ), characterized by the presence of fatigue striations, as shown in Fig. 1.13. However, in the clad alloy, cracks tend to initiate at or near the clad/matrix interface along the fastener hole, as shown in Fig. 1.14[61].

1.5 Corrosion study of 7075 Al alloy

The presence of magnesium- and iron-rich intermetallic impurity particles in 7075 aluminum alloys contributes to corrosion pit formation due to the electrochemical potential difference between these particles and the surrounding matrix. Additionally, these particles can facilitate fatigue crack initiation and propagation, as they are more brittle than the matrix and act as stress concentrators[62,63]. 7075 aluminum alloys achieve their highest strength in the peak-aged condition due to precipitation strengthening[64]. However, they remain susceptible to environmental embrittlement across all aging conditions[44].

In pure aluminum and alloys containing coherent and semi-coherent precipitates that do not disrupt the passive oxide film, pitting corrosion is believed to occur via the breakdown of this protective layer[65]. The breakdown is triggered by chloride ion adsorption, leading to film weakening and dissolution. This process allows chloride and hydrogen ions to interact with the exposed aluminum matrix, promoting localized corrosion[42]. The resulting high concentration of aluminum corrosion by-products further lowers the pH within the pit, accelerating the process. Initially, aluminum dissolves in the chloride solution to form Al^{3+} , which subsequently hydrolyzes into

$AlOH^{2+}$. These species then react with chloride ions to form various aluminum chloride complexes before ultimately hydrolyzing into aluminum hydroxide.

Furthermore, interactions between the matrix and inclusion particles, such as anodic Mg_2 Si or cathodic Al_7 Fe_2 Cu, in regions of a weakened passive film can intensify localized corrosion, leading to pit formation and fatigue crack initiation [12]. Specifically, cross-sectional studies and fractographic analyses indicate that sharp protrusions in localized pit regions create stress concentrations, leading to localized plasticity and premature crack initiation. Additionally, these protrusions are often linked to the shape of corrosion products, and the volume changes they undergo can contribute to microcrack formation within the matrix [3,13]. Fractographic observations of corrosion-pitted aluminum alloys have also revealed multiple fatigue crack initiation sites [10], implying that the presence of several pits may lead to synergistic interactions influencing crack initiation and growth. Recently, X-ray tomography has become a valuable tool for three-dimensional analysis of microstructural damage mechanisms. In situ synchrotron X-ray tomography is also providing insights into corrosion damage evolution, demonstrating that initial damage morphology depends on inclusions and the alloy's rolling [6,10].

Table 1.2: Literature review on corrosion study of 7075 Al alloy

Author	**Material**	**Findings**
Tianjian Yuet al;[48]	7075 Al alloy	• The 7075 aluminum alloy is strengthened using the ultrasonic surface rolling process (USRP), with adjustments to the process parameters made to control the microstructure. • The surface grains of the USRP sample are refined, and the surface SKP (scanning Kelvin probe) potential initially shifts in a positive direction, then gradually decreases as the distance from the surface increases. • The USRP treatment reduces surface roughness and re-dissolves the η-$MgZn_2$ phase, which decreases the initiation sites for pitting corrosion in 7075 Al alloy, leading to a lower density of corrosion pits.
Xing Qiet al;[66]	7075 aluminum alloy	• The impact of ageing treatment on the corrosion behavior of 7075 aluminum alloy coated with micro-arc oxidation (MAO) has been studied. • The MAO coating thickness follows the order: OA (over aged) > PA2(second peak aged 128 h at 120℃ > UA (under aged) > PA1(first peak aged 36 h at 120℃), whereas porosity decreases in the opposite direction. • The coating on OA-treated specimens, characterized by the greatest thickness and lowest porosity, offers the most effective corrosion protection.
Bo Jiang et al;[67]	7075 Al alloy	• The impact of non-isothermal creep aging (NICA) on the microstructure, mechanical properties, and stress corrosion cracking (SCC) resistance of 7075 alloy was examined. • The strength and resistance to stress corrosion cracking (SCC) increased during the heating and cooling phases. Alloys that underwent creep aging at 210 °C followed by cooling to 120 °C (CC120) demonstrated the highest strength and superior SCC resistance. • In alloy CC120, the solutes were more uniformly distributed, which reduced the driving force for electrochemical corrosion.

		More notably, the Cu content in the grain boundary precipitates (GB-ppts) of CC120 showed a slight increase.
Shaopeng Menget al;[68]	7075 aluminum alloy	• The impact of femtosecond laser modification (FLM) on the surface integrity of 7075 aluminum alloy was examined, followed by an evaluation of the samples' electrochemical corrosion behavior in a 3.5% NaCl solution. • The 7075 aluminum alloy was thoroughly examined. FLM induces plastic deformation on the alloy's surface, leading to a notable enhancement in surface mechanical properties, including hardness and residual stress. Furthermore, reducing the spot spacing results in higher surface microhardness, increased roughness, and greater compressive residual stress following FLM. • The results indicate that the hydrophobic texture and the amorphous oxidative layer formed after FLM significantly enhance corrosion resistance. These factors reduce the solid-liquid contact area on the surface, preventing water molecules and halide ions from reaching and penetrating the material. Additionally, the residual stress field generated also contributes to the corrosion resistance following FLM.
Ming Yang et al;[69]	7075 T6 Al alloy	• The influence of a gradient nanostructure, produced through ultrasonic surface rolling, on the stress corrosion behavior of 7075-T6 aluminum alloy was investigated. • The improvement in SCC(stress corrosion cracking) resistance of USRP specimens was primarily attributed to grain refinement, the transformation of the intracrystalline precipitates from the GP zone to the η' phase, and the precipitation of the η phase at trigonal grain boundaries, which reduced the continuous distribution of grain boundary precipitates.
Mengting Zouet al;[70]	7075-T6 Al alloy	• An anodized 7075-T6 aluminum alloy was post-treated in three distinct lithium salt solutions (Li2CO3, Li2C2O4, or LiNO3) under optimized conditions to enhance the alloy's corrosion resistance in both neutral

		NaCl (0.05 M, pH = 6.5) and acidified NaCl (0.6 M, pH = 3.5) solutions. • The alloy specimens treated with lithium salt, irrespective of the type of lithium salt, demonstrated excellent corrosion resistance in a neutral NaCl environment. • The $Li_2C_2O_4$-based alloy sample showed the highest performance in a neutral NaCl environment, attributed to the enhanced compactness of the anodic film and the presence of Li–Al hydroxides in the sealing products.
Bo Zhou et al;[71]	Recycled 7075 Al-alloy	• This paper investigates the smelting, extrusion, and heat treatment processes of recycled 7075 aluminum alloy. It examines the composition, microstructure, mechanical properties, and corrosion resistance of the recycled 7075 aluminum alloy. • After homogenization, solid solution, and aging treatment, the recycled 7075 aluminum alloy plates exhibit a more uniform distribution, finer grain structure, and improved overall quality. • The recycled 7075-T6 aluminum alloy plates exhibit strong resistance to salt spray corrosion. Under continuous exposure to neutral salt spray, the corrosion of these plates begins with pitting and progressively develops into denudation.
Ping Zhang et al;[72]	7075 Al alloy	• This study explores how deep cooling duration and corrosion time influence the surface quality, elemental distribution, corrosion product films, and electrochemical behavior of 7075 aluminum alloy. • Compared to the PM microbial corrosion environment, the 7075-T6 aluminum alloy exhibited a larger charge transfer arc radius in the BM microbial corrosion environment.
Yuqin Rao et al;[73]	Cold spray 7075 Al alloy	• The plasma electrolytic oxidation (PEO) process was applied to deposit an alumina coating on a cold-sprayed 7075 aluminum alloy to enhance its surface properties. • The electrochemical corrosion resistance of the cold-sprayed 7075 aluminum alloy was significantly enhanced by PEO treatment,

		resulting in a three-order reduction in corrosion current density and a more positive corrosion potential.
Mingyu Zhu et al;[74]	7075-T6	• This study investigates the influence of varying frequencies 100 Hz, 200 Hz, 400 Hz, and 600 Hz on the coatings of plasma electrolytic oxidation (PEO) • Taking into account the overall impact of frequency on the thermal control and corrosion resistance of the coatings, 400 Hz was chosen as the optimal parameter for preparing the PEO coating, achieving a high emissivity of 0.858 and a high impedance value of 1.81×10^7 $\Omega \cdot cm^2$.
Lei Bao et al;[75]		• Localized corrosion pitting was observed on the surface of all shot-peened samples. The initiation of pitting corrosion occurred primarily at areas with greater surface roughness. Compared to single shot peening, dual shot peening reduced both the number and depth of corrosion pits. The average pit depths were 14.91 μm for DSP1(dual shot peening with shot dia. 0.18 mm) and 11.09 μm for DSP2(dual shot dia. with shot dia. 0.045 mm. • All samples exhibited intergranular cracking due to stress corrosion. The dual shot peening process produced a higher compressive residual stress and achieved a more uniform surface finish with comparatively lower roughness than the single shot peening process.

Table 1.3: Literature review on effect of corrosive environment on mechanical property of 7075 Al alloy

Author	**Material**	**Findings**
Shijie He et al;[76]	7075 aluminum alloy	• With an emphasis on the development and distribution of η (MgZn2) and η' precipitates, this study examines how artificial ageing affects the mechanical characteristics and corrosion behaviour of 7075 aluminium alloy. • Because of the fine, uniformly distributed η' precipitates and discontinuous GBPs, the results show that the peak-aged condition (13 h) provides the best compromise between corrosion resistance and mechanical performance. • On the other hand, the solution-treated and over-aged states show larger corrosion current densities and deeper pits, which are associated with increased dislocation activity and the development of coarse cathodic intermetallics (Al_7Cu_2 2Fe, Mg_2Si).
Swapna Dey et al;[77]	7075 aluminium alloy	• This study examines how pitting corrosion affects the fatigue life of 7075 aluminium alloy, which is frequently utilised in ageing aircraft constructions. To comprehend their vulnerability to pitting and ensuing fatigue life, the study focusses on two temper conditions, T6 and T73. • The findings showed that the T6 temper was more susceptible to pitting than the T73 temper • When the fatigue lives of T6 and T73 temper were compared under both unpitted and pre-pitted conditions, it was found that T6 had a lower average fatigue life than T73. However, following pre-pitting, the T6 temper showed a higher normalised life than the T73 temper when comparing normalised fatigue life based on the same percentage of yield stress.
Zihao Guo et al; [78]	7075-T6 Al alloy	• In order to investigate the stress corrosion cracking (SCC) behaviour of 7075-T6 aluminium (Al) alloy in a 3.5 weight percent NaCl solution under both elastic and plastic

		strain, this study used a specially made three-point bending (TPB) stress fixture. • Under higher stress levels, tensile stress accelerated corrosion, increased the density of corrosion currents, and decreased the alloy's potential. On the alloy surface, corrosion pits had a higher propensity to expand, group together, and start cracks perpendicular to the tension. • Furthermore, selective anodic dissolution of the Al matrix or anodic IMPs was observed, along with corrosion pits and stress concentration phenomena primarily surrounding intermetallic particles (IMPs).
Meng Liu;[79]	Cold-rolled 7075 Al alloy	• It was investigated how the solution treatment affected the cold-rolled 7075 aluminium alloy's mechanical characteristics and electrical conductivity. • 30 minutes, 60 minutes, 90 minutes, and 120 minutes were the solution times, and the temperatures were 460, 470, 480, and 490 degrees Celsius. The solid solution-aging alloy sheet's tensile strength, yield strength, and hardness first rise and subsequently fall with increasing solution temperature and time • There was a consistent rising trend in the electrical conductivity. An appropriate solution method improves the 7075 aluminium alloy's mechanical characteristics and electrical conductivity.
Zhenglei Yu;[80]	7075 Al/TC4 alloy	• In this study the 7075 Al alloy made with laser powder bed fusion (L-PBF) technology is unable to meet mechanical and corrosion resistance standards because of its coarse columnar grains and severe thermal cracking. • The alloy's ultimate tensile strength of 369.204 MPa and its mechanical characteristics were greatly enhanced. • The corrosion resistance of the alloy was significantly improved, as seen by the corrosion current density dropping from 9.096E-06 to 2.089E-06.

Fig. 1.15 shows that the number and size of corrosion pits in the OA (over aged) state are significantly greater than those in the UA (under aged) state, indicating that the OA state exhibits lower corrosion resistance[42].

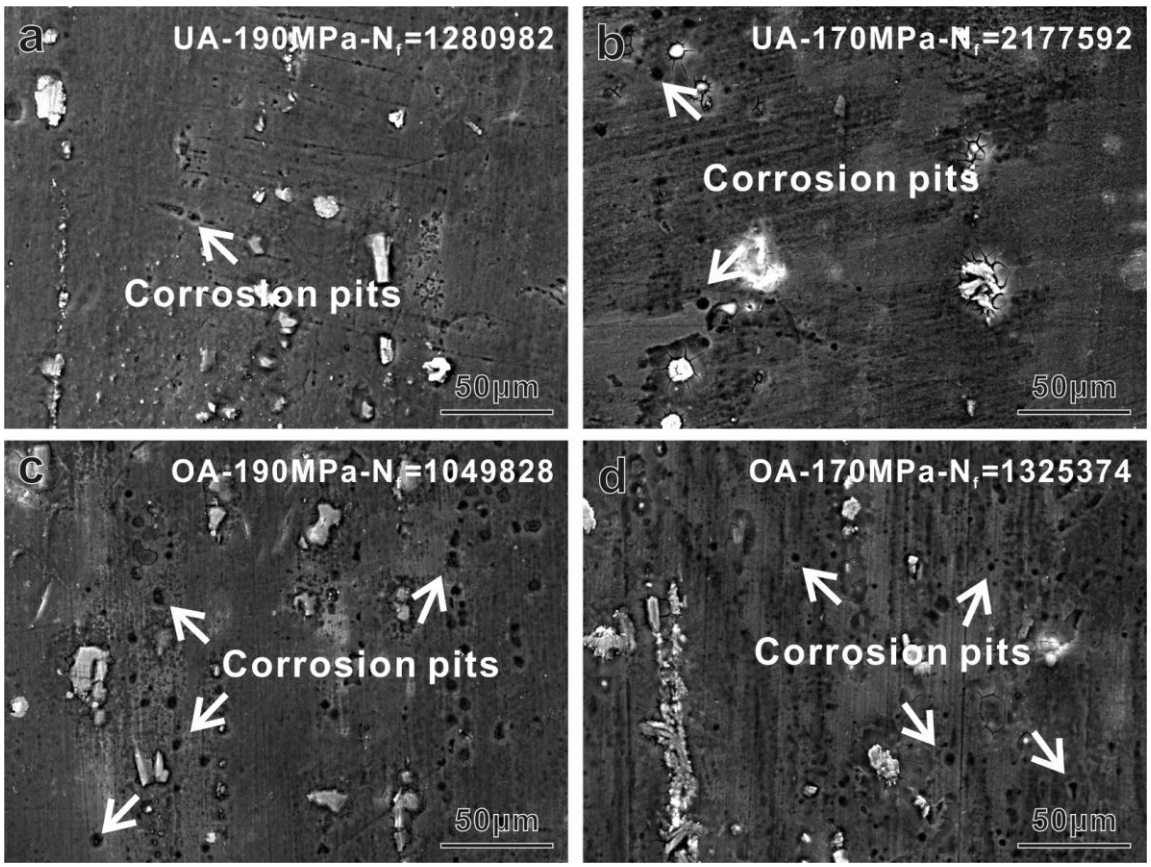

Fig. 1.15 Surface morphologies of the samples of 7075 at different aging states observed by SEM. (a) and (b) UA; (c) and (d) OA[42].

Fig. 1.16 presents the surface morphologies of the CG, 3-passes-DG, 3-passes-DG-U, 7-passes-NG, and 7-passes-NG-U samples after immersion in a 3.5% NaCl solution for 120 hours. Among them, the CG sample showed the most severe corrosion, characterized by numerous deep corrosion pits and noticeable surface peeling (Fig. 1.16(a)). In contrast, the 3-passes-DG sample displayed a limited number of shallow pits with no evident peeling (figs. 1.16 (c) and (d)). The 7-passes-NG sample maintained a largely intact surface with minimal visible corrosion pits (Fig. 1.16 (f)), indicating that USRP treatment significantly enhanced the corrosion resistance of the

7075 Al alloy. However, the 3-passes-DG-U sample showed corrosion cracks and a greater extent of continuous pits compared to the untreated 3-passes-DG sample, suggesting an increase in corrosion severity (Fig. 1.16 (b)). Meanwhile, the 7-passes-NG-U sample, despite undergoing residual stress relaxation, still retained good corrosion resistance with only a few corrosion pits observed (Fig. 1.16 (e)). These findings suggest that the 7-passes-NG sample with a nanocrystalline surface exhibited the highest corrosion resistance among all the samples tested[69].

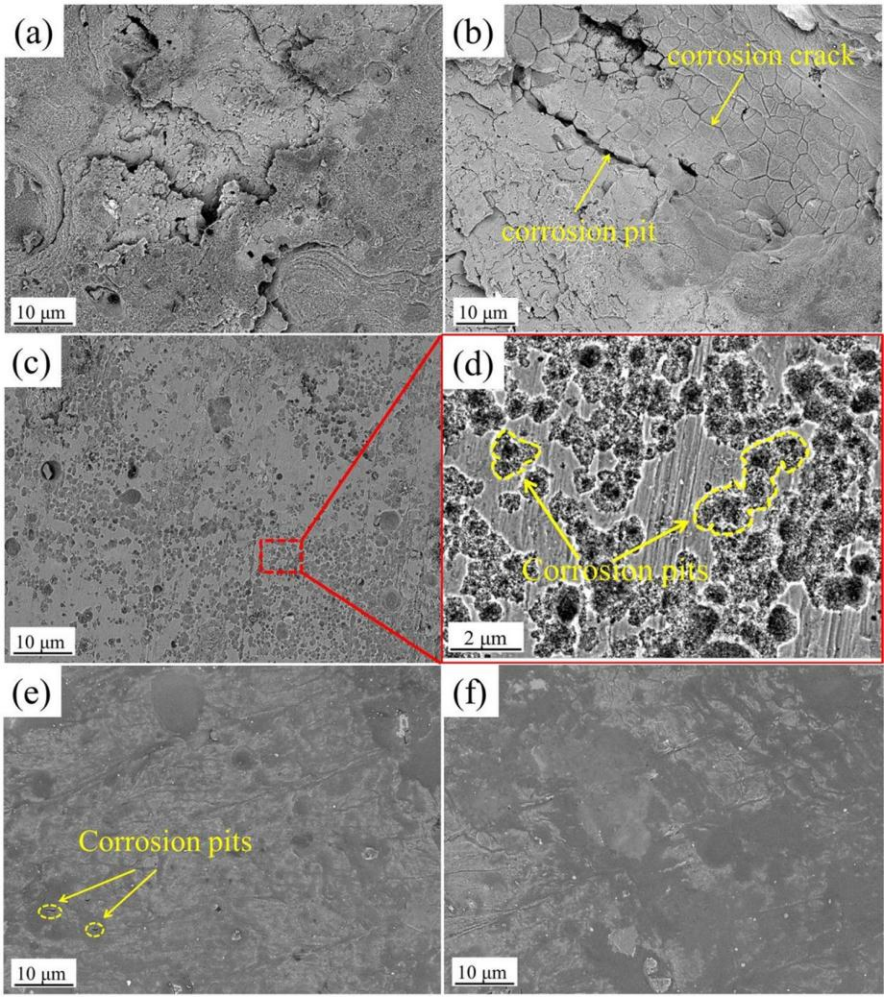

Fig. 1.16 Surface corrosion morphology of 7075 Al alloy after immersion testing:(a) Coarse-Grained (CG); (b) 3-pass Deformed-Grain with Uniaxial rolling (3-passes-DG-U); (c) 3-pass Deformed-Grain (3-passes-DG); (d) Enlarged view of (c); (e) 7-pass

Nanograined with Uniaxial rolling (7-passes-NG-U); (f) 7-pass Nanograined (7-passes-NG)[69].

Fig. 1.17 illustrates the 7075 Al alloy samples before and after ultrasonic surface rolling process (USRP) treatment. Samples exposed to a non-corrosive environment are shown in Fig. 1.17(a), (c), and (e), while those subjected to a corrosive chloride environment are shown in Fig. 1.17(b), (d), and (f). In Fig. 1.17(a) and (b), the untreated sample exhibits coarse grains and a rough surface. Under chloride exposure, deep corrosion pits form, indicating severe surface degradation. After three passes of USRP, as seen in Fig. 1.17(c), grain refinement is minimal. However, in the corrosive environment (Fig. 1.16(d)), only shallow corrosion pits are observed, attributed to reduced surface roughness and increased compressive residual stress. With seven USRP passes, as shown in Fig. 1.17(e), the grains are refined to the nanoscale, precipitates dissolve, and the precipitate-free zone (PFZ) disappears. Correspondingly, Fig. 1.17(f) shows the treated surface has almost no corrosion pits. The formation of a dense passive film is promoted by the high density of grain boundaries due to nanocrystallization, facilitating the rapid enrichment of passive elements. Additionally, the absence of precipitates and the PFZ suppresses anodic dissolution.

Therefore, the key factor enhancing corrosion resistance is the transformation of the surface into a nanostructured layer, which significantly improves the overall corrosion performance of the 7075 Al alloy.

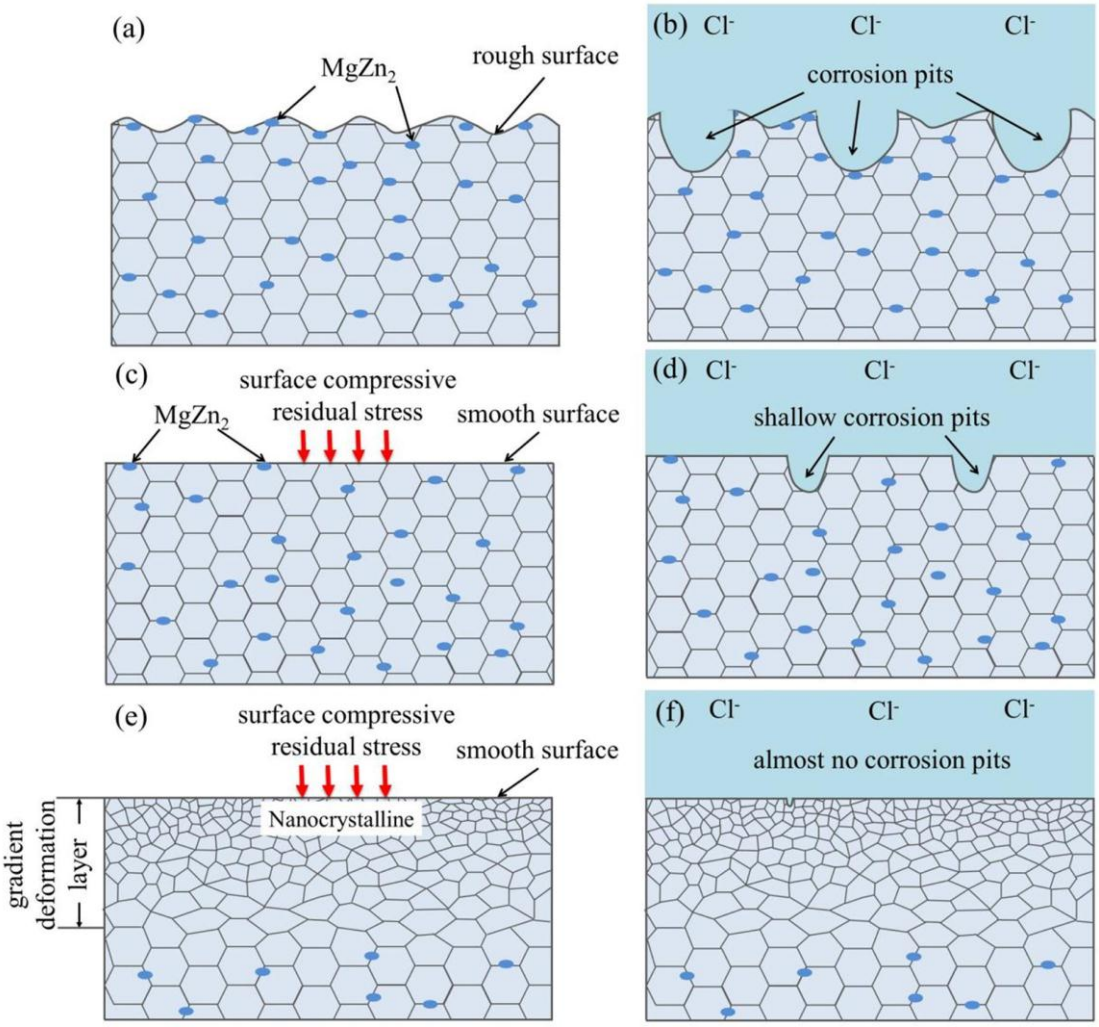

Fig. 1.17 presents the electrochemical corrosion results[69].

Li K et al; [81] examined the influence of TiB_2 on intergranular corrosion (IGC) and exfoliation corrosion (EXCO) in TiB_2 /7075 composites. Prior to conducting Electrochemical Impedance Spectroscopy (EIS) and potentiodynamic polarization tests, all samples were immersed in the test solution for 10 minutes to stabilize, during which the open circuit potential (OCP) was recorded, as shown in Fig.1.18(a).The OCP curves indicate that the 7075-3.5TiB_2 and 7075-7TiB_2 composites demonstrate higher stability compared to the unreinforced 7075 alloy. Potentiodynamic polarization curves are shown in Fig. 1.18(b). Corrosion current density (Icorr) was derived using a nonlinear fitting approach within the weak polarization region of the curves, with

further details provided in the Supplementary Materials. The extracted values of corrosion potential (Ecorr) and Icorr are summarized in Table 1.4. In terms of OCP and Ecorr, the incorporation of 3.5 wt.% TiB_2 particles leads to a reduction in corrosion tendency due to the more positive potential values relative to the 7075 alloy. However, increasing the TiB_2 content to 7 wt.% results in lower OCP and Ecorr, indicating higher corrosion susceptibility. When compared to the base 7075 alloy, the Icorr values decrease by approximately 23% and 75% for the 3.5 wt.% and 7 wt.% TiB_2 composites, respectively.

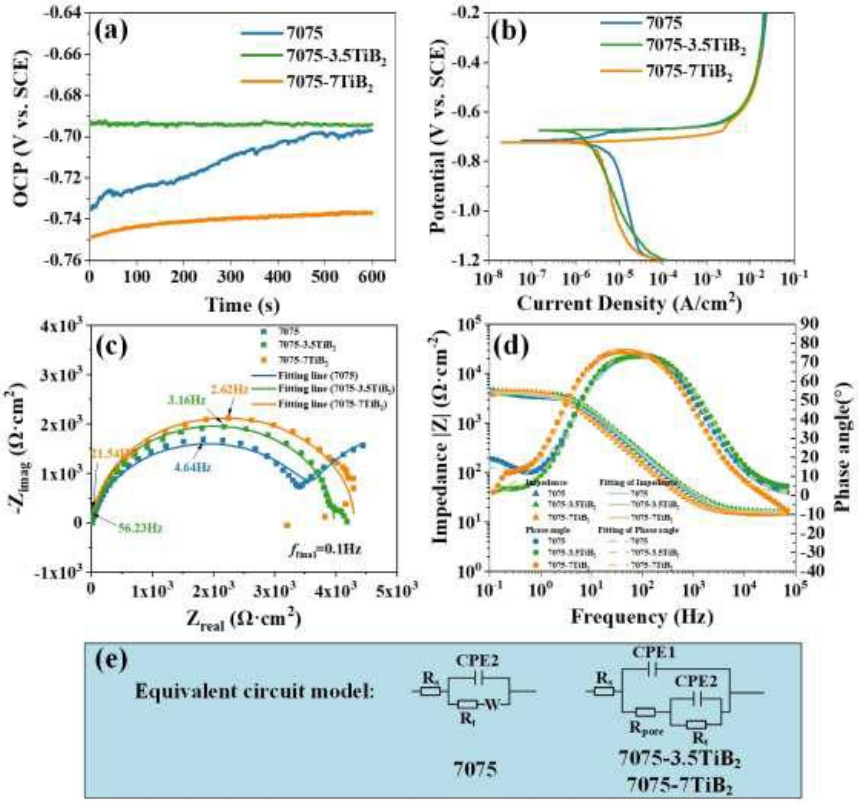

Fig. 1.18 Electrochemical corrosion analysis of the 7075 alloy, 7075–3.5TiB_2 composite, and 7075–7TiB_2 composite:(a) Open Circuit Potential (OCP) curves, (b) Potentiodynamic polarization curves, (c) Nyquist plots, (d) Bode plots showing impedance and phase versus frequency, (e) Equivalent circuit models used to fit the Nyquist data[81].

The equivalent electrical circuit models shown in Fig. 1.18(e) were employed to fit the EIS data. In these circuits, Rs denotes the solution resistance between the sample and the reference electrode. Rpore corresponds to the resistance provided by the corrosion products, while Rt represents the charge transfer resistance. The elements CPE1 and CPE2 are constant phase elements, associated with the corrosion product layer and the electric double layer, respectively. The parameters n1 and n2 are their corresponding dispersion coefficients, and W refers to the Warburg impedance. The capacitance of the electric double layer (CPE2) was calculated using Brug's formula[82], and the capacitance of CPE1 was obtained following literature methods [83].

As shown in Table1. 4, the combined resistance (Rt + Rpore) increased by 15% and 25% with the incorporation of 3.5 wt.% and 7 wt.% TiB_2 , respectively, suggesting that the presence of TiB_2 particles enhances corrosion resistance [83]. The circuit fitting results align well with both the EIS and polarization curves. The increase in Rt is mainly attributed to the higher electrical resistance introduced by the TiB_2 reinforcement. The nearly identical Rs values for the base alloy and the composites indicate good experimental consistency. Fig. 1.18(d) displays Bode plots showing impedance and phase angle variations with frequency. In the Nyquist plot of the 7075 alloy, Warburg impedance is evident in the low-frequency region.

Two electrochemical reactions occur during testing [84]:

$$O_2 + 2H_2O + 4e^- \rightarrow 4OH^-$$

$$Al + 3OH^- \rightarrow Al(OH)_3 + 3e^-$$

Table 1.4 Electrochemical corrosion behavior parameters[81]

Corrosion parameters	**7075**	**7075-3.5TiB2**	**7075-7TiB2**
Ecorr vs.SCE (V)	0.717±0.031	0.674±0.024	0.722±0.019
Icorr (μA/cm2)	9.2±0.3	7.1±0.7	2.3±0.1
Rs (Ω·cm2)	16.27	16.07	15.55
Rpore (Ω·cm2)	-	263.8	370.1
Rt (Ω·cm2)	3435	3690	3918
Rpore+ Rt (Ω·cm2)	3435	3953.8	4288.1
Y01 (Ω-1·cm-2·sn, ×10-6)	-	7.33	12.07
n1	-	0.94	0.96
CPE1 (F·cm-2, ×10-6)	-	4.92	6.87
Y02 (Ω-1·cm-2·sn, ×10-6)	13.34	2.54	4.4
n2	0.90	0.94	0.91
CPE2 (F·cm-2, ×10-6)	5.24	1.59	2.31
W (Ω-1·cm-2·s0.5, ×10-6)	859	-	-
χ2(×10-3)	2.72	1.87	4.63

1.6 Current challenges and literature gap

- Difficulty in cold rolling of 7075 Al alloy
- Very limited studies are available regarding elastic plastic J_{1c} fracture toughness and fatigue crack growth behavior of 7075 Al alloy in normal condition and in corrosive environment

1.7 Objectives

- To optimized the cold rolling process of 7075 Al alloy.
- To study elastic plastic J_{1c} fracture toughness value and fatigue crack growth rate behavior of 7075 Al alloy in normal environment
- To study elastic plastic J_{1c} fracture toughness value and fatigue crack growth rate behavior of 7075 Al alloy in corrosive environment